

Automated Modeling Method for Pathloss Model Discovery

Ahmad Anaqreh, Shih-Kai Chou, Mihael Mohorčič, Thomas Lagkas, Carolina Fortuna

Abstract—Modeling propagation is the cornerstone for designing and optimizing next-generation wireless systems, with a particular emphasis on 5G and beyond era. Traditional modeling methods have long relied on statistic-based techniques to characterize propagation behavior across different environments. With the expansion of wireless communication systems, there is a growing demand for methods that guarantee the accuracy and interpretability of modeling. Artificial intelligence (AI)-based techniques, in particular, are increasingly being adopted to overcome this challenge, although the interpretability is not assured with most of these methods. Inspired by recent advancements in AI, this paper proposes a novel approach that accelerates the discovery of path loss models while maintaining interpretability. The proposed method automates the formulation, evaluation, and refinement of the model, facilitating the discovery of the model. We examine two techniques: one based on Deep Symbolic Regression, offering full interpretability, and the second based on Kolmogorov-Arnold Networks, providing two levels of interpretability. Both approaches are evaluated on two synthetic and two real-world datasets. Our results show that Kolmogorov-Arnold Networks achieve the coefficient of determination value R^2 close to 1 with minimal prediction error, while Deep Symbolic Regression generates compact models with moderate accuracy. Moreover, on the selected examples, we demonstrate that automated methods outperform traditional methods, achieving up to 75% reduction in prediction errors, offering accurate and explainable solutions with potential to increase the efficiency of discovering next-generation path loss models.

Index Terms—machine learning, automated discovery, pathloss, interpretability, kolmogorov-arnold network, symbolic regression

I. INTRODUCTION

DISCOVERING accurate and interpretable scientific formulas that align with established theories is a fundamental goal in science. Traditionally, scientists formulate a hypothesis, derive formulas manually to test it, relying exclusively on theoretical knowledge or statistical characteristics, and subsequently verify its accuracy through simulations and experiments. However, this manual approach, which excludes experimental data during the discovery phase, can be time-consuming. Automated methods have emerged to overcome this limitation by incorporating data directly into the discovery process in several disciplines [1], [2]. Thus, accurate and interpretable formulas are generated, significantly improving both the speed and quality of the modeling process compared to traditional methods. For instance, recent work in high-energy physics [3] has demonstrated that symbolic regression (SR) can derive models from experimentally measured data

that closely resemble the Tsallis distribution, a well-known statistical distribution.

Unlike AI scientists [4], that aim to even replace humans in the scientific discovery process, automated methods aim to support the human user to be able to discover interpretable relationships directly from data, without relying on predefined models, by seeking functional representations that capture the underlying patterns [5]. Figure 1 illustrates both manual and automated modeling approaches. In manual methods, experts derive formulas based on existing theories, then evaluate and refine them through hands-on analysis. In contrast, automated methods use data to model patterns, which are subsequently evaluated and refined in an automated manner. Note that the solid line denotes intensive iteration, while the dashed line indicates limited iteration. By leveraging tools such as evolutionary strategies [6] and neural network architectures [7], these methods can efficiently model complex relationships.

Understanding specific electromagnetic propagation models is paramount for wireless networks that have been engineered over time by humans and enable our everyday communication needs. Our ability to build and understand these networks hinges on understanding and modeling how signals are attenuated when propagating through space in realistic environments [8]. Pathloss (PL) models describe the attenuation behavior of signal propagation in various wireless communication systems, incorporating essential factors such as frequency, distance, and presence of various obstacles along the path [9]. Over the years, a variety of methods have been proposed for modeling PL, including empirical, deterministic, and machine learning-based approaches, each with its strengths and limitations [8], [10]. In recent years, such models have been modeled with deep neural networks (DNNs) [11], in some cases showing better results than some existing analytical models and classical machine learning-based models [10]. However, models based on DNNs are inherently difficult to interpret and explain [12], which hinders the ability to teach humans the principles and intuitions behind models.

In order to enable scientists and engineers to have more efficient PL model discovery tools while maintaining human interpretability, in this paper, we propose a novel approach that accelerates the discovery of PL models. Motivated by the observation that PL models often involve logarithmic functions in their expression [8], and recognizing that such functions can present challenges for certain model discovery techniques [5], we investigate an alternative method with different levels of interpretability.

The contributions of this paper are outlined as follows.

- 1) We propose a new PL model discovery approach that automates the model formulation, evaluation, and refinement, facilitating model discovery. In particular, we consider Deep Symbolic Regression (DSR), offering

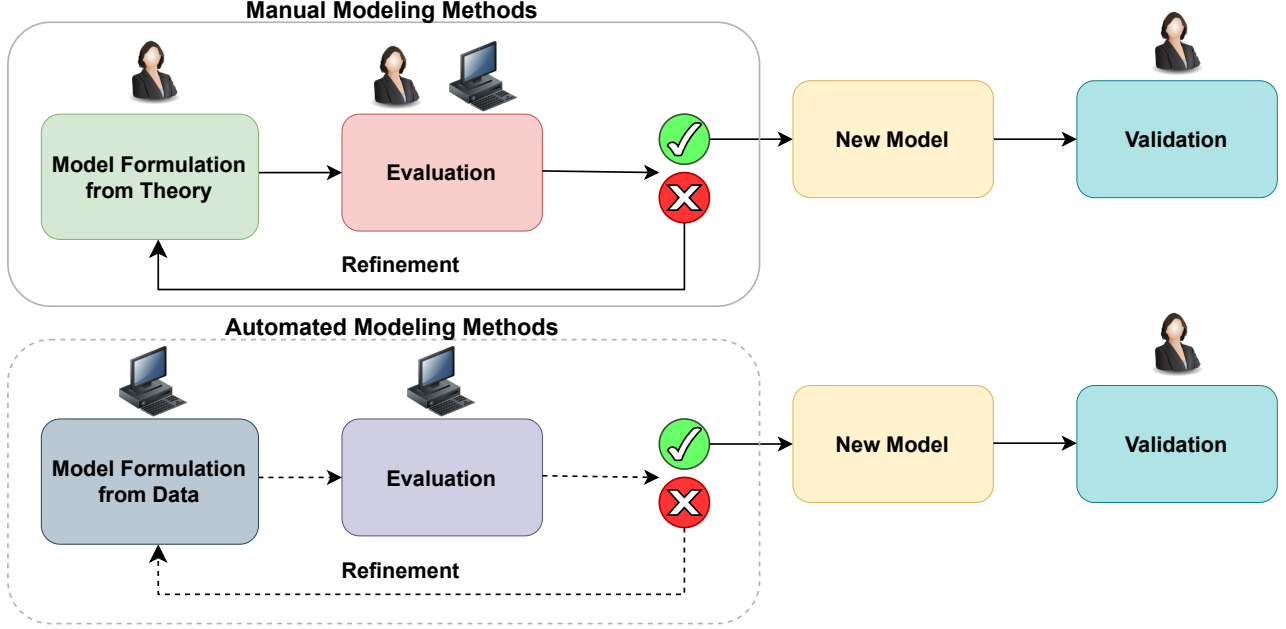


Fig. 1: Comparison of modeling methods.

full interpretability, and Kolmogorov-Arnold Networks (KANs), providing two flavors of interpretability, as candidate automation techniques.

- 2) Our results show the feasibility of the proposed automation method on two synthetic and two real-world datasets. More specifically, we show that KANs achieve R^2 values close to 1 with minimal prediction error, while DSR generates compact models with moderate accuracy.
- 3) On the selected examples, we demonstrate that automated methods outperform traditional methods, achieving up to 75% reduction in prediction errors, offering accurate and explainable solutions with potential to increase the efficiency of discovering path loss models for the next-generation wireless communication systems.
- 4) We provide the automatic KAN-based model discovery workflow for all scenarios as open source¹.

The paper is organized as follows: Section II provides a review of the relevant literature, followed by a description of the problem in Section III. Section IV details the methods employed to address the problem, while Section V details the training data and training methodologies. Section VI presents the results. Finally, Section VII concludes the paper and discusses potential future research directions.

II. RELATED WORK

In this section, we first summarize related work regarding automated scientific discovery, followed by related works on AI for PL modeling.

A. Automating Scientific Discovery

Perhaps the most recent trend in automating scientific discovery is to develop AI systems that are able to automate every step of the process, including idea generation, full experiment iteration and paper write up [4]. Slightly more developed, but still in very early stages of research, various approaches to automating hypothesis generation and verifications have been proposed [13].

SR is one of the earliest and most widely used modeling techniques. A breakthrough came with the introduction of genetic programming (GP), which refines mathematical expressions using evolutionary operations such as mutation, crossover, and selection [6]. GP has been extensively used in SR and remains a dominant approach due to its ability to discover compact expressions [14]. However, GP has significant computational challenges, particularly when searching through large, high-dimensional function spaces [15]. As the complexity of mathematical expressions increases, the search space expands exponentially, resulting in challenges such as local optima, slow convergence, and insufficient global search guidance. These difficulties have driven the development of hybrid approaches that integrate deep learning and reinforcement learning (RL) with SR, aiming to improve efficiency and exploration.

Mundhenk et al. [16] introduced a neural-guided genetic programming (NGGP) approach, where a recurrent neural network generates initial populations for GP. Unlike standard GP, NGGP uses a trained neural network to initialize the GP search with higher-quality candidate expressions, leading to faster convergence. A closely related approach, Genetic Expert-Guided Learning (GEG) [17], combines priority queues and GP to select high-quality expressions for RL. However, GEG

¹<https://github.com/sensorlab/AutoPathloss>

uses only one evolutionary step per training iteration, which limits the depth of genetic refinement.

Other hybrid models integrate RL to adjust mutation probabilities, guide selection criteria, or optimize hyperparameters dynamically [18], [19]. These approaches introduce mechanisms to bias evolutionary search toward higher-reward expressions, helping GP escape local optima while maintaining structural consistency in generated formulas. Another class of hybrid approaches interchanges populations between GP and neural models. Pourchot et al. [20] and Khadka et al. [21] applied population interchange in deep reinforcement learning tasks such as robotic control. These approaches demonstrate that GP-generated expressions can be used to refine neural network policies while neural models can improve the diversity of GP populations.

Recent advances in deep learning have introduced alternative methods for SR. Kusner et al. [22] proposed GrammarVAE, which uses a variational autoencoder to model symbolic expressions as latent-space representations while enforcing syntactic constraints. However, the method struggles with recovering exact expressions and often generates invalid mathematical structures. The approach proposed in [23] incorporates SR into a neural network architecture, where activation functions represent symbolic operators. This approach requires strong assumptions about the functional form of the target equation, which limit its flexibility. A major advancement came with AI Feynman [24], which combines neural networks with symbolic rule discovery to simplify expressions before applying SR. AI Feynman successfully identifies symmetries and separable functions in data, allowing it to break down complex problems into smaller, easier-to-learn subproblems. However, it does not perform a direct symbolic search, making it unsuitable for some real-world applications.

RL-based approaches have demonstrated notable improvements, particularly in terms of accuracy and convergence speed. One of the key challenges in RL is the efficient sampling of promising expressions. Importance sampling, first introduced by Glynn & Iglehart [25], has been adapted in RL-based approaches to prioritize high-reward expressions while reducing computational cost. Another powerful optimization technique is the cross-entropy method (CEM) [26], which has been widely used in RL for sampling high-quality solutions from a probabilistic distribution. These approaches have helped address the exploration-exploitation trade-off, ensuring meaningful expressions without excessive random exploration.

KANs [27] represent a significant advancement and shift in neural network design by enhancing the ability to model complex data relationships while maintaining high accuracy and interpretability. The KANs architecture plays a crucial role in achieving these benefits across various domains. Xu et al. [28] applied KANs to time series forecasting, introducing T-KAN and MT-KAN, which demonstrated improved predictive performance by effectively capturing temporal dependencies. De Carlo et al [29] developed the Graph Kolmogorov-Arnold Network (GKAN), integrating spline-based activation functions into graph neural networks, leading to enhanced accuracy and interpretability in tasks like node classification and link prediction. Bozorgasl & Chen [30] proposed Wav-KAN, in-

corporating wavelet functions into KANs to efficiently capture both high and low frequency components, improving accuracy and robustness, particularly for multiresolution analysis. By design, KANs enable more interpretability compared to other DNNs as they learn the composition of splines that approximate the data. By looking at the learned graph and the splines at each nodes, one can interpret what has been learned from the data and why. More recently, they have been extended with symbolic functionality where an actual expression can be extracted from the graph by approximating the learned splines with known functions [31].

B. AI for Pathloss

To date, our preliminary PL approximation study is the first work to consider interpretable AI modeling of wireless networks [32]. Several works on explainable AI for various aspects of 6G have been proposed, as surveyed in [33]. In some cases, the developed models also claim interpretability, or "local" interpretability, however, depending on the work, the term refers either to a visual illustration of how much importance a model assigns to certain features or how a deep learning network activates, i.e., activation maps. Of course, certain classical machine learning models, also referred to as "transparent models" in [33], such as regression trees or linear regression, are also interpretable; however, they tend to yield less accurate models.

With respect to AI-aided PL modeling, [11] proposed a meta-learning approach based on DNNs to develop a PL prediction model when only sparse measurements are available. However, its superiority compared to conventional techniques is not immediately clear. On the other hand, [10] showed that a fully connected network was superior to a boosted tree model and two conventional approaches in several scenarios.

III. PROBLEM STATEMENT

The guiding hypothesis of this work is the possibility of automating the formulation, evaluation, and refinement steps of the conventional PL model development process. By doing so, the aim is to equip scientists and engineers with more efficient tools for discovering PL models and, at the same time, maintaining human interpretability. In order to validate this hypothesis, we consider two classes of models: analytical and empirical. The two considered analytical models are PL^{ABG} (Alpha-Beta-Gamma) and PL^{CI} (Close-in) models [34], which are widely used in modeling PL in wireless systems. The two empirical models, herein referred to as PL^{EI} and PL^{EO} , correspond to indoor and outdoor environments, respectively, and have been developed from measurements in [35]. As analytical baselines for corresponding PL models, we include the indoor multiwall-and-floor (PL^{MWF}) and outdoor free space (PL^{FS}) models. Based on the data generated with the analytical and baseline models, as well as the empirically measured one, we aim to automatically learn the most likely expression, i.e., formulas, that best describe the respective PL.

A. ABG and CI Analytical Models

The ABG and CI models are particularly used for describing signal propagation in urban micro- and macro-cellular scenarios, incorporating frequency, distance, and shadowing factors.

The ABG model is defined by the equation:

$$PL^{\text{ABG}}(f, d) = 10\alpha \log_{10} \left(\frac{d}{1 \text{ m}} \right) + \beta + 10\gamma \log_{10} \left(\frac{f}{1 \text{ GHz}} \right) + \chi^{\text{ABG}}, \quad (1)$$

where $PL^{\text{ABG}}(f, d)$ is the path loss in dB, α and γ are coefficients that represent the dependence on distance (d) and frequency (f) respectively. β is an optimized offset value for the path loss, and χ^{ABG} represents the standard deviation of the shadow fading.

The CI model is described by the equation:

$$PL^{\text{CI}}(f, d) = FSPL(f, 1 \text{ m}) + 10n \log_{10}(d) + \chi^{\text{CI}}, \quad (2)$$

where n is the path loss exponent (PLE), d is the transmitter-receiver distance in three dimensions, $FSPL(f, 1 \text{ m})$ is the free-space path loss at 1 meter and χ^{CI} represents the shadow fading. $FSPL(f, 1 \text{ m})$ is computed as follows:

$$FSPL(f, 1 \text{ m}) = 20 \log_{10} \left(\frac{4\pi f}{c} \right), \quad (3)$$

where c is the speed of light.

B. The Indoor and Outdoor Empirical Models

El Chall et al. [35] derived empirical PL models for LoRaWAN (Long-Range Wide Area Network) based on extensive field measurements conducted in Lebanon. Indoor experiments were carried out at Saint Joseph University, while outdoor experiments were performed in Beirut City. The collected data were analyzed using linear regression to derive PL models for both indoor and outdoor environments.

For indoor environments, they proposed the following PL model:

$$PL^{\text{EI}}(d) = 10n \log_{10}(d) + PL_0 + n_w L_w + n_f^{\left(\frac{n_f+2}{n_f+1}-b\right)} L_f, \quad (4)$$

where $n = 2.85$ is the path loss exponent, $PL_0 = 120.4$ is the reference PL, $b = 0.47$ is a fitting parameter, $L_f = 10$ and $L_w = 1.41$ are the attenuation factors for floors and walls, respectively.

The PL model for outdoor environments is given by:

$$PL^{\text{EO}}(d) = 10n \log_{10}(d) + PL_0 + L_h \log_{10}(h_{\text{ED}}) + X_\sigma, \quad (5)$$

where L_h denotes the additional loss related to the antenna height h_{ED} . The parameters obtained from the fitting process are: PL exponent $n = 3.119$, reference PL $PL_0 = 140.7$, and antenna height loss factor $L_h = -4.7$, $X_\sigma = 9.7$ is a zero-mean Gaussian random variable representing shadow fading.

C. The Baseline Multiwall-and-Floor and Free Space Models

To describe PL within buildings, it is essential to incorporate the additional attenuation caused by walls and floors. Therefore, the PL can be defined as:

$$PL^{\text{MWF}}(d) = 10n \log_{10}(d) + PL_0 + \text{WAF} + \text{FAF}, \quad (6)$$

where d is the distance between the transmitter and the receiver, $\text{WAF} = n_w L_w$ and $\text{FAF} = n_f L_f$ represent the wall and floor attenuation factors, which are determined by the number of walls n_w and floors n_f traversed. Based on the empirical models discussed in Section III-B, the PL exponent is $n = 2.85$, with a reference PL of $PL_0 = 120.4$. The attenuation factors are $L_f = 10$ for floors and $L_w = 1.41$ for walls.

The Free Space model is a baseline approach used to estimate PL when the transmitter and receiver have a clear line-of-sight without any obstacles, defined as follows:

$$PL^{\text{FS}}(f, d) = 20 \log_{10}(f) + 20 \log_{10}(d) + 32.44, \quad (7)$$

IV. METHODOLOGIES

For automating the PL modeling of the models identified in Section III, and to further validate the working hypothesis, we identify two automated modeling methods capable of learning a symbolic representation from the data at hand: the recently introduced KANs and DSR.

The design decision to adopt KANs as candidate techniques for enabling the automation of PL learning is justified by the shortcomings of typical techniques in learning logarithmic functions [5]. Knowing that existing PL models often involve logarithmic functions in their expression [8], KANs may have superior performance in approximating such models while being able to produce two flavors of interpretability.

A. Kolmogorov-Arnold Networks

KANs have recently emerged as an alternative to multi-layer perceptron (MLP) based architectures, demonstrating strong performance on scientific tasks while maintaining interpretability. KANs have strong mathematical foundations based on the Kolmogorov-Arnold representation theorem, which states that any multivariate continuous function can be expressed as a sum of univariate functions [27]. KANs and MLPs implement activation functions in fundamentally different ways: KANs have activation functions on edges, while MLPs have activation functions on nodes. This unique design allows KANs to provide a more transparent and interpretable mapping between inputs and outputs, enhancing explainability while preserving the model's ability to capture complex patterns.

The structure of a KAN can be represented as $[n_1, \dots, n_{L+1}]$, where L denotes the total number of layers. A deeper KAN is constructed by composing L layers as follows:

$$Y = \text{KAN}(X) = (\Phi_L \circ \Phi_{L-1} \circ \dots \circ \Phi_1)X. \quad (8)$$

Each layer of a KAN is represented by a matrix in which each entry is an activation function. If a layer contains d_{in}

nodes and its adjacent layer has d_{out} nodes, the layer can be expressed as a $d_{in} \times d_{out}$ matrix Φ of activation functions:

$$\Phi = \{\phi_{q,p}\}, p = 1, 2, \dots, d_{in}, q = 1, 2, \dots, d_{out}. \quad (9)$$

KAN utilizes the SiLU activation function combined with B-splines to enhance expressiveness. In this setup, edges control the transformations between layers, while nodes perform simple summation operations. A B-spline of order k requires $G + k$ basis functions to define the spline over a given grid. Consequently, for each input (node in a layer), evaluating a B-spline of order k involves computing $G + k - 1$ basis functions and performing a weighted sum with the corresponding control points:

$$\text{spline}(x) = \sum_{i=0}^{G+k-1} c_i B_i(x). \quad (10)$$

B. Deep Symbolic Regression

At the core of DSR [7] are the representation of mathematical expressions as sequences, the development of an autoregressive model to generate these expressions, and the use of a risk-seeking policy gradient approach to train the model to produce more accurate and well-fitting expressions.

The sequence generator defines a parameterized distribution over mathematical expressions, $p(\tau \mid \theta)$. The model is typically designed to ensure computational tractability of expression likelihoods for the parameters θ , allowing for back-propagation with a differentiable loss function. A common implementation is a recurrent neural network (RNN), where the likelihood of the i -th token (τ_i) is conditionally independent of other tokens, given the initial ones ($\tau_1, \dots, \tau_{i-1}$). This is expressed as:

$$p(\tau_i \mid \tau_{j \neq i}, \theta) = p(\tau_i \mid \tau_{j < i}, \theta). \quad (11)$$

The sequence generator is generally trained using RL or related techniques. From this perspective, the sequence generator works as a RL policy to be optimized. This process involves sampling a batch of N expressions \mathcal{T} , evaluating each expression using a reward function $R(\tau)$, and applying gradient descent to minimize a loss function. In this work, we employ three approaches to train the RNN.

1) *Risk-Seeking Policy Gradient (RSPG)*: Originally proposed in [7], this approach prioritizes optimizing the best-case reward rather than the average. The loss function is defined as:

$$\mathcal{L}(\theta) = \frac{1}{\epsilon |\mathcal{T}|} \sum_{\tau \in \mathcal{T}} (R(\tau) - \tilde{R}_\epsilon) \nabla_\theta \log p(\tau \mid \theta) \mathbf{1}_{R(\tau) > \tilde{R}_\epsilon}, \quad (12)$$

where ϵ is a hyperparameter controlling the level of risk-seeking, \tilde{R}_ϵ is the empirical $(1 - \epsilon)$ quantile of the rewards in \mathcal{T} , and $\mathbf{1}$ is an indicator function.

2) *Vanilla Policy Gradient (VPG)*: This method employs the REINFORCE algorithm [36], where training is performed over the batch \mathcal{T} with the loss function:

$$\mathcal{L}(\theta) = \frac{1}{|\mathcal{T}|} \sum_{\tau \in \mathcal{T}} (R(\tau) - b) \nabla_\theta \log p(\tau \mid \theta), \quad (13)$$

where b is a baseline term, such as an exponentially weighted moving average (EWMA) of rewards.

3) *Priority Queue Training (PQT)*: Proposed by Abolafia [37], this non-RL approach focuses on optimizing best-case performance. It stores samples from each batch in a maximum reward priority queue (MRPQ), and training is conducted on these stored samples using a supervised learning objective:

$$\mathcal{L}(\theta) = \frac{1}{k} \sum_{\tau \in \text{MRPQ}} \nabla_\theta \log p(\tau \mid \theta), \quad (14)$$

where k is the size of the MRPQ.

For a pre-order traversal τ and a dataset of (X, y) pairs of size N , where $X \in \mathbb{R}^n$ and $y \in \mathbb{R}$, the normalized root-mean-square error (NRMSE) is defined as:

$$\text{NRMSE}(\tau) = \frac{1}{\sigma_y} \sqrt{\frac{1}{N} \sum_{i=1}^N (y_i - f(X_i))^2}, \quad (15)$$

where $f : \mathbb{R}^n \rightarrow \mathbb{R}$ is the mathematical expression instantiated from τ , and σ_y is the standard deviation of y . Thus, the reward function is described as:

$$R(\tau) = \frac{1}{1 + \text{NRMSE}(\tau)}. \quad (16)$$

V. EVALUATION METHODOLOGIES

To ensure full replicability of the entire study and elaborate on the setup under which the evaluation has been done, in this section, we first discuss the type of data used to train the automatic discovery methods, followed by the training methodologies for each method.

A. Training Data

1) *Synthetic Data*: The dataset was generated following the approach described in [32] to approximate the PL models defined by Eq. (1) and Eq. (2) in Section III-A. The parameter ranges, summarized in Table I, were derived from authentic data in studies that comprehensively analyze various scenarios and frequency ranges, highlighting the applicability of PL^{ABG} and PL^{CI} models in various contexts [9], [34], [38]. Specifically, for PL^{ABG} the parameters $\alpha, \gamma, \beta, f, d$, and χ were used as inputs, while for PL^{CI} f, n, d , and χ were the inputs. The dataset consists of 1,000 instances. The frequency was converted to hertz for the PL^{CI} , following standard practice in the literature.

TABLE I: The parameters and their corresponding values for PL^{ABG} and PL^{CI} .

Parameter	ABG	CI
α	[0.1, 2.5]	-
β	[-10, -1]	-
γ	[0, 2]	-
$f(\text{GHz})$	[2, 73.5]	[2, 73.5]
$d(m)$	[1, 500]	[1, 500]
χ	[4, 12]	[4, 12]
n	-	[2, 6]

2) *Empirically Measured Data*: Measurements were conducted in two distinct environments, indoor and outdoor, as described in [35]. The indoor dataset includes 1,317 instances, and the outdoor dataset contains 787 instances. Input parameters for PL^{EI} included n_w , n_f , d , and f , while the PL^{EO} used h_{ED} , d , and f . The corresponding parameter ranges are presented in Table II. For performance evaluation, we compared the automated methods with the models described in Section III-B and developed by the authors in [35] using the real-world measurements².

TABLE II: The parameters and their corresponding values for PL^{EI} and PL^{EO} .

Parameter	EI	EO
n_w	[0, 3]	-
n_f	[1, 4]	-
$f(MHz)$	[868.1, 868.5]	[868.1, 868.5]
$d(m)$	[6.47, 105.25]	[27.66, 170.44]
$h_{ED}(m)$	-	[0.2, 3]

3) *Analytical Baselines*: The PL^{MWF} model, defined in Eq. (6), was used as the baseline for the indoor environment, whereas the PL^{FS} model, defined in Eq. (7), was employed as the baseline for the outdoor scenario.

B. Training of KANs

We use the original KAN implementation from the pykan library³ and train the KANs in a similar way as other ML models, using the 80-20 split of data as depicted in Figure 2. During training, various configurations of layers and grid sizes are varied to optimize performance. In this process, the splines and weights of the edges connecting these splines, as described in Section IV-A, are learned. Unlike MLPs, KANs are not very deep (i.e., usually about 3 layers with 5 being very deep) and not very wide [27]. Due to their relative shallowness and narrowness, once learned, they can be visualized as a graph with the learned activation functions overlaid on the edges and the importance of compositions represented as edge weight. This alone already gives more intuition on the learned model than in the case of other neural architectures. However, as a second step, a mechanism to match the learned splines with actual known functions also exists. We perform default automated matching relying on the library's default *auto_symbolic()* functionality. After the matching step, the network is retrained with the respective functions by only updating the weights of the edges. Finally, a fully interpretable symbolic formula is extracted as a last step in the training. To tune the KANs, we perform a full grid search for each model with grid size $grids \in \{5, 8, 10, 15, 20, 30, 40, 50\}$, $steps \in \{50, 100, 200, 300\}$ and $lambda \in \{0.02, 0.002, 0.0002, 0.00002\}$. The final tuned hyperparameters for the PL models learned by KANs are summarized in Table III. For both the CI and ABG models, we normalize the training data to maintain consistency with our previous work [32]. In preliminary experiments without normalization, the frequency, expressed in hertz in the CI

model, tended to dominate the other input variables, resulting in imbalanced feature contributions.

TABLE III: Tuned hyperparameters for KANs.

Layers	Grid	Steps	k	λ
ABG model				
[6, 6, 1]	10	100	3	0.002
CI model				
[4, 4, 1]	8	300	3	0.002
Indoor model				
[4, 1]	5	100	3	0.0002
Outdoor model				
[3, 1]	50	100	3	0.02

C. Training of DSR

We used the DSR implementation provided by the deep_symbolic_optimization library⁴, by training it in a manner consistent with standard machine learning models. Specifically, we employ 80% of the data for training and 20% for testing. The flow diagram for DSR method is illustrated in Figure 3. As depicted in the figure, RNN generates symbolic expressions from the training data while adhering to predefined constraints. RL guides the process by assigning a reward to each expression based on its fit to the training data. Using the policy gradient methods, introduced in Section IV-B, the RL algorithm updates the RNN parameters to iteratively improve the generated expressions. This process continues until a stopping criterion, such as convergence or a performance threshold, is met. Finally, the best symbolic expression is obtained.

In DSR, a set of constraints can be implemented to narrow the search space, ensuring the generation of meaningful expressions while preserving computational efficiency. The following constraints were specifically applied. **Expression Length Limits**: Expressions were constrained to a minimum length of 4 to avoid trivial solutions and a maximum length of 40 to maintain interpretability. **Avoiding Redundant Constants**: Operators were restricted to prevent all their children from being constants, preventing the generation of expressions that simplify to a single constant. **Unary Operator Consistency**: Unary operators were restricted from having their inverse as a child (e.g., $\log(\exp(x))$) to prevent the generation of redundant expressions. **Trigonometric Operator Composition**: Trigonometric operators were restricted from having other trigonometric operators as descendants (e.g., $\sin(1 + \cos(x))$) to prevent unnecessary complexity, despite being mathematically valid. **Repeat Constraint**: This constraint regulates the occurrence of specific tokens (e.g., operators and/or variables) in generated expressions by enforcing minimum and maximum limits. It softly penalizes violations of the minimum threshold to allow exploration while strictly invalidating expressions that exceed the maximum limit. The repeat constraint with f and d was utilized in all cases.

Each of the three RNN-based algorithms (RSPG, PQT, and VPG) has one unique algorithm-specific parameter, for which we adopted default values as presented in [7], i.e. the risk

²<https://zenodo.org/records/1560654>

³<https://github.com/KindXiaoming/pykan>

⁴<https://github.com/dso-org/deep-symbolic-optimization>

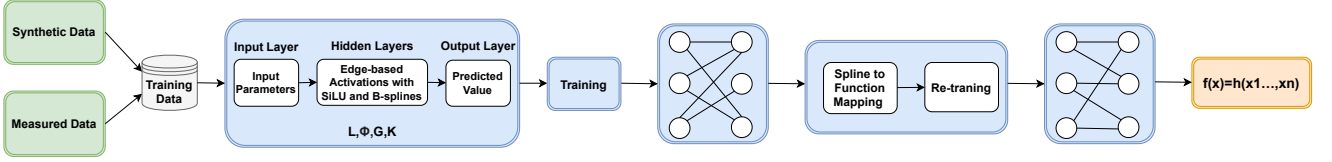


Fig. 2: The flow diagram of developing a pathloss model using KANs.

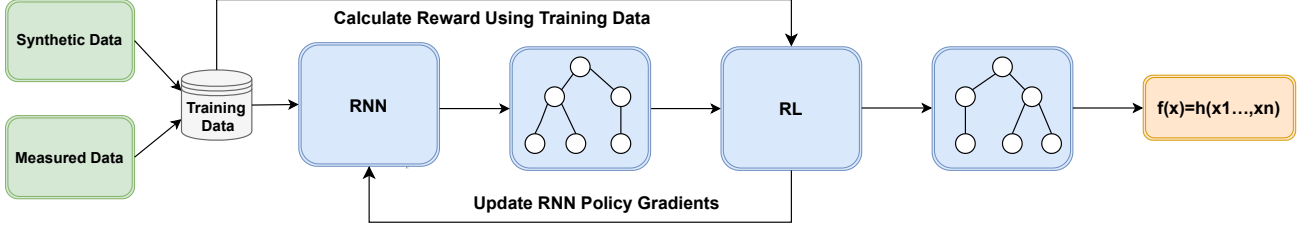


Fig. 3: The flow diagram of developing a pathloss model using DSR.

factor ($\epsilon = 0.05$) for RSPG, the priority queue size ($k = 10$) for PQT, and the EWMA coefficient ($\alpha = 0.25$) for VPG. In addition to these unique parameters, all three algorithms share a common set of hyperparameters (batch size, learning rate and entropy weight). We explored various values for these hyperparameters to achieve the best performance. The final tuned hyperparameters are summarized in Table IV.

TABLE IV: Tuned hyperparameters for RNN-based algorithms in DSR.

Parameter	RSPG	PQT	VPG
ABG model			
Batch size	200	200	200
Learning rate	0.002	0.002	0.0001
Entropy weight	0.008	0.005	0.005
CI model			
Batch size	200	200	200
Learning rate	0.001	0.002	0.0005
Entropy weight	0.008	0.005	0.008
Indoor model			
Batch size	300	200	200
Learning rate	0.0005	0.001	0.001
Entropy weight	0.03	0.01	0.02
Outdoor model			
Batch size	200	200	200
Learning rate	0.0005	0.0005	0.0001
Entropy weight	0.01	0.01	0.01

D. Evaluation Metrics

The performance of the modeling methods was evaluated using four key metrics: Mean Absolute Error (MAE), Mean Squared Error (MSE), Mean Absolute Percentage Error (MAPE), and the coefficient of determination (R^2). MAE measures the average absolute difference between the predicted and actual values. MSE emphasizes larger errors by squaring the deviations. MAPE expresses prediction accuracy as a percentage of actual values, providing a normalized measure that allows for meaningful comparison. Finally, R^2 quantifies the proportion of variance in the actual values by indicating how well the predictions capture the variability present in the actual values.

VI. EVALUATION RESULTS

In this section, we evaluate the efficiency of the methods introduced in Section IV to address the problem outlined in Section III, using the methodologies described in Section V. We provide a discussion with a summary of the findings at the end of the section.

A. Learning the ABG Model from Synthetic Data

The performance comparison for KAN and DSR methods on the PL^{ABG} is presented in Table V. The KAN [6,6,1] achieves superior predictive performance, with exceptionally low error metrics (MAE = 0.06, MSE = 0.01, MAPE = 0.28) and R^2 value of 1, indicating a nearly perfect alignment between the model predictions and the actual data as confirmed by the plot in Figure 4. In the figure, *pred* stands for the predicted PL values and *true* stands for the actual values based on Eq. (1). In contrast, the KAN [6,6,1] Auto-symbolic, which replaces the learned splines with known functions and re-learns new weights for the edges of the graph, shows significantly lower accuracy, with MAE = 3.89, MSE = 28.14, MAPE = 12.51, and $R^2 = 0.93$. Among DSR models, DSR-RSPG obtained the best performance (MAE = 3.86, MSE = 33.50, MAPE = 14.28, $R^2 = 0.92$), followed by DSR-PQT (MAE = 5.90, MSE = 62.07, MAPE = 21.83, $R^2 = 0.90$) and DSR-VPG (MAE = 6.67, MSE = 83.38, MAPE = 20.48, $R^2 = 0.77$). These results highlight that while KAN [6,6,1] achieves the highest accuracy, other methods show varying performance metrics, generally with higher error rates and lower values of R^2 .

As discussed in Sections IV-A and V-B, KANs learn splines and weights on the edges, and the best configuration is found using grid search. In our experiments, the best KAN architecture learned for PL^{ABG} is depicted in Figure 5 and has a three-layer design [6, 6, 1]. The first layer includes six input nodes, corresponding to the parameters $\alpha, \gamma, \beta, f, d, \chi$; the second layer has the same number of nodes, and the output layer consists of a single node representing the predicted value

TABLE V: Performance comparison on ABG model.

Methods \ Metrics	MAE	MSE	MAPE	R ²	Expression
KAN [6,6,1]	0.06	0.01	0.28	1	Tree and splines in Fig. 5
KAN [6,6,1] Auto-symbolic	3.89	28.14	12.51	0.93	$-291.519 \log_{10}(8.686 - 3.052\alpha) + 32.175 \cos(1.116\gamma - 1.323) + 9.005\beta -$ $53.258 \log_{10}(9.367 - 3.859d) + 0.016(0.028f - 1)^2 + 313.289 -$ $\frac{0.476}{(-f - 0.168)^2} + 8.008\chi$
DSR-RSPG	3.86	33.50	14.28	0.92	$20\alpha + 10\gamma + \beta + \log_{10}(d) + \frac{\gamma f}{10} + \chi$
DSR-PQT	5.90	62.07	21.83	0.90	$20\alpha + 15\gamma + \beta + \frac{f}{20} + \chi$
DSR-VPG	6.67	83.38	20.48	0.77	$(\alpha + \gamma)(10 + \chi)$

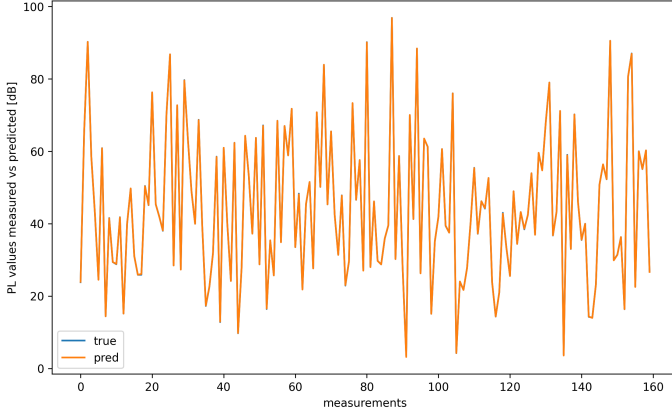


Fig. 4: The predicted values by the KAN model vs the actual generated by PL^{ABG} according to Eq. (1) as per parameters in Table I.

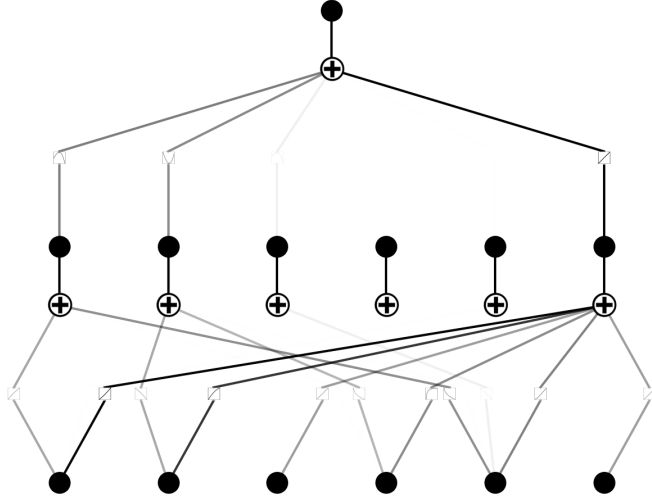
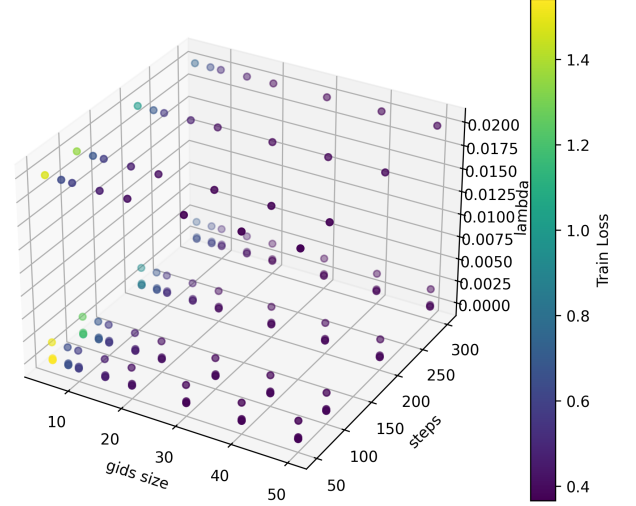


Fig. 5: The learned KAN [6,6,1] network for approximating PL^{ABG} .

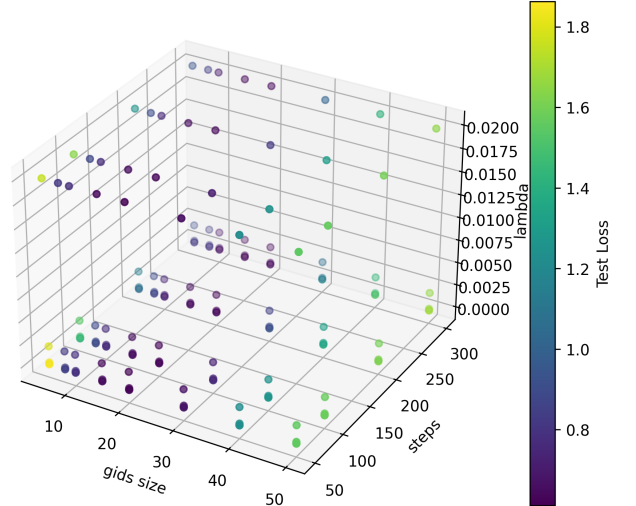
of the function. This architecture was selected based on the smallest train losses and test losses during the grid search to find this model. The result of the grid search is illustrated in Figure 6 (a and b), showing how variations in these parameters affect test loss and train loss, with color gradients illustrating

3D Scatter: gids size vs steps vs lambda (Train Loss as color)



(a) Train loss (the smaller, the better).

3D Scatter: gids size vs steps vs lambda (Test Loss as color)



(b) Test loss (the smaller, the better).

Fig. 6: Parameter search for the KAN [6,6,1] architecture for approximating PL^{ABG} .

the scale of the losses.

It can be seen from the learned graph in Figure 5 that the final expression is the summation of four terms, with the third

one having a lower weight, i.e. very light gray coloring of the edge that connects the hidden layer with the output layer. It can also be observed from the functions learned on the first three edges of the last layer of the graph that they perform a non-linear transformation, while the last one performs a linear one. From the coloring of the edges and summations in the hidden layer, the first summation node, a quasi-linear transformation of α is summed with a non-linear transformation of d with medium weighting. In the second summation node, a medium weighted quasi-linear transformation of γ with a non-linear transformation of f . The next three summation nodes have low to minimal weighting, while the last summation node aggregates all six inputs with high to medium weights.

Finally, we examine the validity of the expressions generated by the KANs and DSR methods. For PL^{ABG} , the expressions obtained by KAN [6,6,1] Auto-symbolic and DSR-RSPG are considered valid, as they correctly represent PL as a function of f and d . We also notice that the expression learned by the KAN [6,6,1] Auto-symbolic is more complex than the one learned by the DSR-RSPG. In contrast, the expression generated by DSR-PQT fails to include d , and the DSR-VPG expression excludes both f and d . These results indicate that the DSR-PQT and DSR-VPG expressions are unlikely to be valid for accurately modeling PL from a communication engineering perspective.

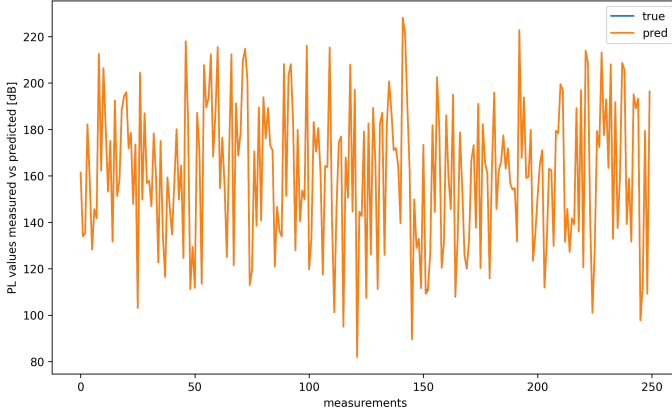


Fig. 7: The predicted values by the KAN model vs the actual generated by PL^{CI} according to Eq. (2) as per parameters in Table I.

B. Learning the CI Model from Synthetic Data

Table VI presents the performance comparison of various methods for discovering PL^{CI} . The KAN [4,4,1] method achieved the best results, with minimal error values (MAE = 0.05, MSE = 0.01, MAPE = 0.04) and an R^2 value of 1, showing a highly accurate fit between the predicted values and the actual values as illustrated in Figure 7. In the figure, *pred* represents the predicted PL values and *true* represents the actual values based on Eq. (2). The KAN [4,4,1] Auto-symbolic showed lower performance, with MAE = 4.56, MSE = 36.26, MAPE = 3.05, and $R^2 = 0.96$. Among the DSR methods, DSR-RSPG yielded the lowest error (MAE = 11.49, MSE = 261.46, MAPE = 10.21, $R^2 = 0.80$), followed by

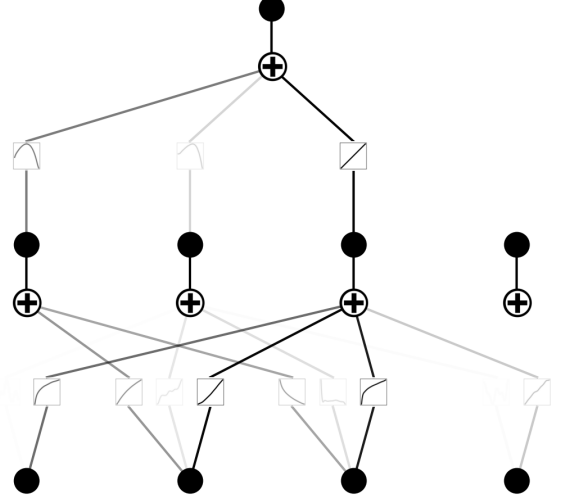


Fig. 8: The learned KAN [4,4,1] network for approximating PL^{CI} .

DSR-PQT (MAE = 13.60, $R^2 = 0.84$) and DSR-VPG (MAE = 16.90, $R^2 = 0.67$). These results demonstrate that the KAN [4,4,1] significantly outperforms the other methods, with smaller errors corresponding to better predictive accuracy.

Figure 8 shows the KAN architecture utilized for PL^{CI} modeling, featuring a three-layer design [4, 4, 1]. The first layer consists of four input nodes corresponding to the parameters f, n, d, χ , followed by a hidden layer with four nodes, and a single-node output layer representing the predicted function value. As before, to optimize the hyperparameters for KAN, we investigated various grid sizes, steps, and lambda values, as shown in Figures 9 (a and b). The 3D scatter plots illustrate how variations in the parameters affect both the train and test loss.

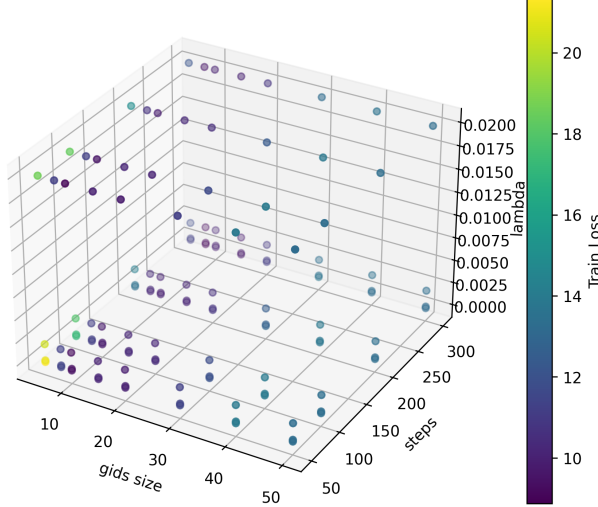
From the learned graph in Figure 8, it can be seen that the final expression is the summation of three terms, where the second one has a lower weight. The functions associated with the first two edges of the last layer apply nonlinear transformations, whereas the third edge performs a quasi-linear transformation. From the coloring of the edges and summations in the hidden layer, it can be observed that, in the first summation node, a quasi-linear transformation of n and a non-linear transformation of d are combined, both with medium weighting. The second summation node aggregates the non-linear transformation of n and d with low weights. Finally, the third summation node aggregates all four inputs with high to medium weights.

The expressions generated by KAN and DSRs for the PL^{CI} demonstrate the validity of those modeled by KAN [4,4,1] Auto-symbolic and DSR-RSPG, as in both cases the PL is appropriately modeled as a function of f and d . We note that, same as in the case of the PL^{ABG} , the expression produced by the KAN [4,4,1] Auto-symbolic is quite complex. The expression generated by DSR-PQT, although it includes both f and d , models the frequency term using $\cos(\log_{10}(f))$. This implies a periodic contribution of f to

TABLE VI: Performance comparison on CI model.

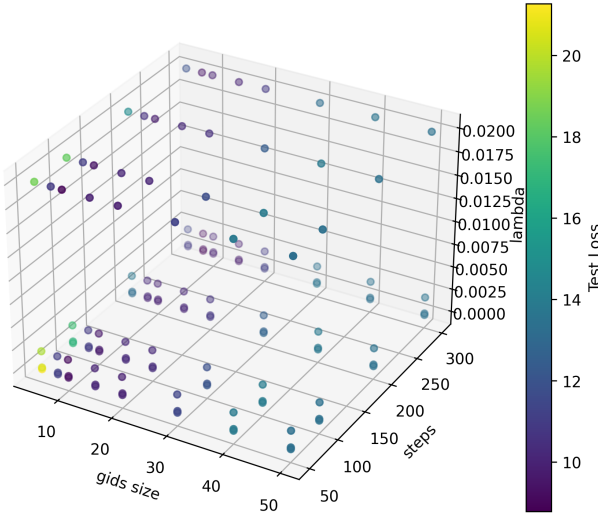
Methods \ Metrics	MAE	MSE	MAPE	R^2	Expression
KAN [4,4,1]	0.05	0.01	0.04	1	Tree and splines in Figure 8
KAN [4,4,1] Auto-symbolic	4.56	36.26	3.05	0.96	$-280.464 \log_{10}(8.729 - 1.621n) + 43.806 \log_{10}(1.064d + 1.913) + 19.929 \log_{10}(5.162f + 9.329) + 50.758 \log_{10}(0.789\chi + 7.457) + 352.246$
DSR-RSPG	11.49	261.46	10.21	0.80	$23n + \frac{d}{10} + \log_{10}(f) + 40$
DSR-PQT	13.60	223.05	10.58	0.84	$23n + \frac{d}{10} + (\chi + n)\cos(\log_{10}(f)) + 40$
DSR-VPG	16.90	570.92	15.24	0.67	$21n + 2\chi + 60$

3D Scatter: gids size vs steps vs lambda (Train Loss as color)



(a) Train loss (the smaller, the better).

3D Scatter: gids size vs steps vs lambda (Test Loss as color)



(b) Test loss (the smaller, the better).

Fig. 9: Parameter search for the KAN [4,4,1] architecture for approximating PL^{CI} .

PL, which contradicts the fundamental characteristics of signal propagation, as PL increases with increasing f . Furthermore, the expression obtained by DSR-VPG excludes both f and d . These results imply the invalidity of the DSR-PQT and DSR-

VPG expressions for the PL modeling.

C. Learning an Indoor Model from Empirical Data

The performance comparison of various methods for modeling PL in an indoor environment is presented in Table VII. The PL^{MWF} serves as the baseline, yielding the highest errors (MAE = 9.01, MSE = 121.54, MAPE = 8.98) and R^2 value of 0.56, indicating a moderate predictive performance. PL^{EI} , based on Eq. (4) from [35], slightly improves accuracy, with MAE = 7.64, MSE = 111.67, MAPE = 7.52, and $R^2 = 0.49$. However, all automated methods outperform both the baseline and the empirical model. KAN [4,1] significantly improves accuracy (MAE = 6.11, MSE = 59.87, MAPE = 6.22) and a substantially higher R^2 value of 0.76, as shown in Figure 10, where $pred$ stands for the predicted PL values and $true$ stands for the actual measurements from [35]. The KAN [4,1] Auto-Symbolic performs similarly, with slightly higher errors but maintaining the same R^2 value. Among DSR methods, DSR-RSPG achieves the overall superior performance (MAE = 5.95, MSE = 55.73, MAPE = 5.96, $R^2 = 0.71$), though its R^2 remains inferior to that of the KAN models. DSR-PQT and DSR-VPG demonstrate comparatively weaker performance, with higher errors and lower values of R^2 (0.65 and 0.57, respectively). Overall, the results highlight that both KANs and DSR models provide substantial improvements over the baseline model and the indoor empirical model.

Figure 11 illustrates the architecture of the KAN [4,1] used for indoor PL prediction. The architecture has two layers; the first layer consists of four input nodes corresponding to the parameters n_w, n_f, d, f , and a single-node output layer representing the predicted value. As illustrated in the figure, the final expression is a sum of four terms, with the fourth term contributing less due to its smaller weight. Notably, the function learned on the first edge applies a non-linear transformation, whereas the remaining three edges implement quasi-linear transformations.

For the indoor environment, the KAN [4,1] Auto-symbolic expression contains a $\cos(f)$ term, implying a periodic dependence on frequency. This contradicts the physical behavior of the signal, as PL increases consistently with f . In contrast, the expression obtained by DSR-RSPG is valid, as it includes both f and d . Furthermore, the findings highlight the invalidity of the expressions of PQT and VPG: the expression of DSR-PQT does not include f , while the expression of DSR-VPG excludes both f and d .

TABLE VII: Performance comparison in an indoor environment.

Methods \ Metrics	MAE	MSE	MAPE	R^2	Expression
PL^{MWF}	9.01	121.54	8.98	0.56	$10n \log_{10}(d) + PL_0 + WAF + FAF$
PL^{EI}	7.64	111.67	7.52	0.49	$10n \log_{10}(d) + PL_0 + n_w L_w + n_f \left(\frac{n_f+2}{n_f+1} - b \right) L_f$
KAN [4,1]	6.11	59.87	6.22	0.76	learned tree and splines as in Figure 11.
KAN [4,1] Auto-symbolic	6.27	61.62	6.38	0.76	$41.516 \log_{10}(0.383d + 4.03) - 1.328 \cos(5.036f - 0.448) + 4.912 \sin(8.226n_w - 2.854) + 52.026 \log_{10}(2.408n_f + 8.63) - 11.236$
DSR-RSPG	5.95	55.73	5.96	0.71	$\frac{d}{2} + 3\log_{10}(f) + 5n_w + 70$
DSR-PQT	7.09	80.99	7.19	0.65	$\frac{d}{2} + 4n_w + 80$
DSR-VPG	7.38	84.11	7.29	0.57	$n_f^2 + 4n_f + n_f n_w + 80$

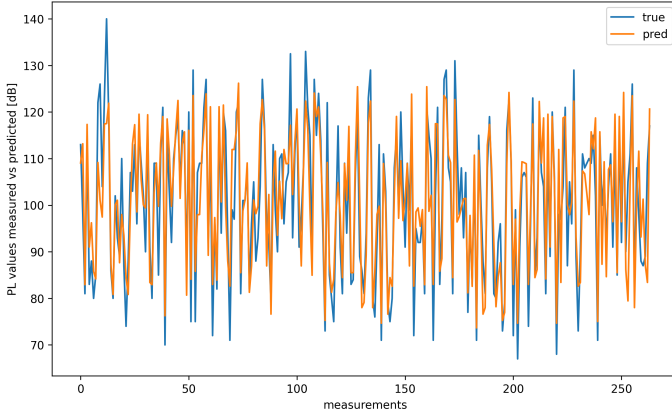
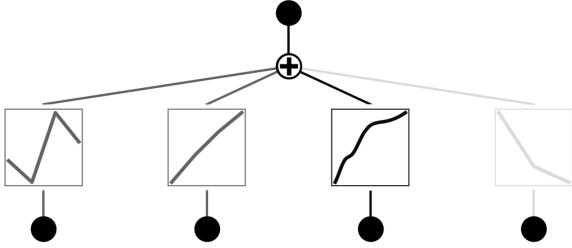


Fig. 10: The predicted values by the KAN model vs the actual indoor measurements.

Fig. 11: The learned KAN [4,1] network for approximating PL^{EI} .

D. Learning an Outdoor Model from Empirical Data

Table VIII summarizes the performance of different methods for PL prediction in an outdoor environment. The PL^{FS} , yields high error values (MAE = 34.08, MSE = 1242.99, MAPE = 31.43) and a low R^2 value of 0.30, indicating poor predictability. The PL^{EO} , represented by Eq. (5) from [35], substantially improves accuracy (MAE = 18.09, MSE = 398.88, MAPE = 17.82), but retains the same R^2 value of 0.30. In contrast, the KAN model [3,1] achieves significantly better performance, with the lowest errors (MAE = 4.59, MSE = 38.59, MAPE = 4.36) and a higher R^2 value of 0.71, as demonstrated in Figure 12 showing the comparison

between predicted and measured PL values. The KAN [3,1] Auto-symbolic yields poor performance (MAE = 9.50, R^2 = 0.01), showing a higher error and a lower fit compared to the original KAN structure. Among the DSR models, DSR-RSPG performs the best (MAE = 6.62, MSE = 72.09, MAPE = 6.31); however, its R^2 value (0.29) remains low. DSR-PQT and DSR-VPG show slightly higher errors and comparable R^2 values. Overall, the KAN [3,1] model outperforms both traditional and DSR methods, offering a more accurate method for outdoor PL prediction.

Figure 13 illustrates the KAN architecture evaluated for the outdoor model, consisting of a two-layer design [3, 1]. The first layer includes three input nodes corresponding to the parameters h_{ED}, d, f , followed by a single output node representing the predicted PL value. The figure shows that the final expression is a sum of three terms, with the first and third terms having smaller weights. It can be observed that the functions learned on the second and third edges apply non-linear transformations, whereas the first implements a quasi-linear transformation.

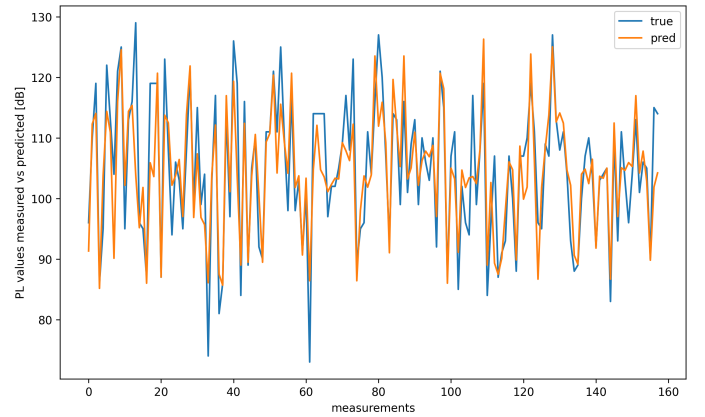
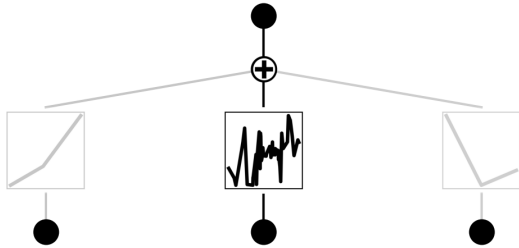


Fig. 12: The predicted values by the KAN model vs the actual outdoor measurements.

The only valid expression for the outdoor environment is obtained from DSR-RSPG, as it includes both f and d . The KAN [3,1] Auto-symbolic expression excludes d and incorporates a cosine function of f . The expression of DSR-PQT excludes f . Finally, although the DSR-VPG expression includes both f and d , it defines f using a sine function, introducing a

TABLE VIII: Performance comparison in an outdoor environment.

Methods \ Metrics	MAE	MSE	MAPE	R ²	Expression
PL^{FS}	34.08	1242.99	31.43	0.30	$20 \log_{10}(d) + 20 \log_{10}(f) + 32.44$
PL^{EO}	18.09	398.88	17.82	0.30	$10n \log_{10}(d) + PL_0 + L_h \log_{10}(h_{ED}) + X_\sigma$
KAN [3,1]	4.59	38.59	4.36	0.71	learned tree and splines as in Figure 13
KAN [3,1] Auto-symbolic	9.50	133.42	9.34	0.01	$0.99 \cos(8.71f - 3.47) - 2.34 \log_{10}(7.68 - 2.16h_{ED}) + 105.74$
DSR-RSPG	6.62	72.09	6.31	0.29	$h_{ED}d + \log_{10}(f) + 80$
DSR-PQT	7.25	80.45	6.78	0.29	$\log_{10}(\frac{d}{h_{ED}}) + \frac{d}{10} + 90$
DSR-VPG	8.18	97.90	7.46	0.28	$\frac{d + \sin(f)}{10} + 90$

Fig. 13: The learned KAN [3,1] network for approximating PL^{EO} .

periodicity that misrepresents the actual relationship between f and PL .

E. Discussion

The evaluation results across ABG, CI, indoor, and outdoor PL modeling scenarios reveal a clear trade-off between the accuracy and the interpretability of expressions generated by KANs and DSR methods.

KANs consistently achieve superior predictive accuracy across all scenarios. For example, KAN [6,6,1] and KAN [4,4,1] achieve exceptionally low error metrics and R^2 values of 1, emphasizing their superior ability to model complex data relationships. The learned models, in the form of spline approximations and weights in a graph composition, are more interpretable compared to deep learning alternatives; however, they are not conventional human-interpretable expressions. To gain insights into the interpretability of the KANs, auto-symbolic is utilized to map from spline-based structures to more interpretable functional forms.

Auto-symbolic variants, such as KAN [6,6,1] Auto-symbolic and KAN [3,1] Auto-symbolic, exhibit invalid expressions, higher error rates, and, in some cases, notably lower R^2 values compared to their original forms. This illustrates the limits of the current mapping capabilities of KANs, resulting in less accurate and interpretable expressions. In contrast, DSR methods, especially DSR-RSPG, generate simple, valid, and interpretable expressions. Although DSR methods achieve a reasonable level of accuracy, their predictive performance is generally outperformed by KANs. The lower values observed in the DSR methods indicate a trade-off in which

predictive precision is reduced to preserve the simplicity and interpretability of the resulting expressions.

In general, our findings indicate that KANs provide highly accurate solutions with higher interpretability compared to typical activation maps of DNNs, but lower than some of the considered DSR methods. On the other hand, DSR methods prioritize interpretability over predictive accuracy. The choice between these methods should be determined by the intended objective, whether to maximize predictive accuracy or to derive interpretable expressions that offer clear analytical insight.

VII. CONCLUSION

The work demonstrates the potential of automated modeling methods, particularly KANs and DSR, to discover accurate and interpretable PL models in wireless communication systems. Through comprehensive evaluation against traditional models such as ABG, CI, and empirical models for outdoor and indoor environments, we demonstrate that KANs consistently achieve superior predictive accuracy across both synthetic and real-world data. Although KANs are less interpretable, they achieve cutting-edge performance. In contrast, DSR generates compact expressions with moderate predictive precision, offering a favorable trade-off between accuracy and interpretability. These results promote the integration of automated methods into the design of next-generation wireless systems, where the demand for efficient and explainable models continues to increase.

In future work, our goal is to focus on enhancing the symbolic mapping mechanisms within KANs for improved interpretability. Furthermore, extending both the KANs and DSR methods to cover diverse scenarios will be essential to validate their robustness and adaptability. These advances have the potential to contribute significantly to the development of intelligent, adaptive modeling frameworks in the field of wireless communication systems.

REFERENCES

- [1] J. Jumper, R. Evans, A. Pritzel, T. Green, M. Figurnov, O. Ronneberger, K. Tunyasuvunakool, R. Bates, A. Žídek, A. Potapenko *et al.*, “Highly accurate protein structure prediction with alphafold,” *nature*, vol. 596, no. 7873, pp. 583–589, 2021.
- [2] M. Schmidt and H. Lipson, “Symbolic regression of implicit equations,” in *Genetic programming theory and practice VII*. Springer, 2009, pp. 73–85.
- [3] N. Makke and S. Chawla, “Data-driven discovery of tsallis-like distribution using symbolic regression in high-energy physics,” *PNAS Nexus*, vol. 3, no. 11, p. pgae467, 10 2024.

- [4] C. Lu, C. Lu, R. T. Lange, J. Foerster, J. Clune, and D. Ha, "The ai scientist: Towards fully automated open-ended scientific discovery," *arXiv preprint arXiv:2408.06292*, 2024.
- [5] N. Makke and S. Chawla, "Interpretable scientific discovery with symbolic regression: a review," *Artificial Intelligence Review*, vol. 57, no. 1, p. 2, 2024.
- [6] J. R. Koza, "Genetic programming as a means for programming computers by natural selection," *Statistics and computing*, vol. 4, pp. 87–112, 1994.
- [7] B. K. Petersen, M. L. Larma, T. N. Mundhenk, C. P. Santiago, S. K. Kim, and J. T. Kim, "Deep symbolic regression: Recovering mathematical expressions from data via risk-seeking policy gradients," in *International Conference on Learning Representations*, 2021.
- [8] C. Phillips, D. Sicker, and D. Grunwald, "A survey of wireless path loss prediction and coverage mapping methods," *IEEE Communications Surveys & Tutorials*, vol. 15, no. 1, pp. 255–270, 2012.
- [9] S. Sun, T. S. Rappaport, T. A. Thomas, A. Ghosh, H. C. Nguyen, I. Z. Kovacs, I. Rodriguez, O. Koymen, and A. Partyka, "Investigation of prediction accuracy, sensitivity, and parameter stability of large-scale propagation path loss models for 5g wireless communications," *IEEE transactions on vehicular technology*, vol. 65, no. 5, pp. 2843–2860, 2016.
- [10] J. Ethier and M. Châteauevert, "Machine learning-based path loss modeling with simplified features," *IEEE Antennas and Wireless Propagation Letters*, 2024.
- [11] S. Zeng, Y. Ji, F. Rong, L. Yang, L. Yan, and X. Zhao, "Meta-pl: Path loss prediction of lte networks at sparse measurement areas using meta-learning," *IEEE Antennas and Wireless Propagation Letters*, 2025.
- [12] R. Dwivedi, D. Dave, H. Naik, S. Singhal, R. Omer, P. Patel, B. Qian, Z. Wen, T. Shah, G. Morgan *et al.*, "Explainable ai (xai): Core ideas, techniques, and solutions," *ACM Computing Surveys*, vol. 55, no. 9, pp. 1–33, 2023.
- [13] R. Cory-Wright, C. Cornelio, S. Dash, B. El Khadir, and L. Horesh, "Evolving scientific discovery by unifying data and background knowledge with ai hilbert," *Nature Communications*, vol. 15, no. 1, p. 5922, 2024.
- [14] F.-A. Fortin, F.-M. De Rainville, M.-A. G. Gardner, M. Parizeau, and C. Gagné, "Deap: Evolutionary algorithms made easy," *The Journal of Machine Learning Research*, vol. 13, no. 1, pp. 2171–2175, 2012.
- [15] G. Kronberger, F. Olivetti de Franca, H. Desmond, D. J. Bartlett, and L. Kammerer, "The inefficiency of genetic programming for symbolic regression," in *International Conference on Parallel Problem Solving from Nature*. Springer, 2024, pp. 273–289.
- [16] T. N. Mundhenk, M. Landajuela, R. Glatt, C. P. Santiago, D. M. Faissol, and B. K. Petersen, "Symbolic regression via neural-guided genetic programming population seeding," in *Proceedings of the 35th International Conference on Neural Information Processing Systems*, 2021, pp. 24912–24923.
- [17] S. Ahn, J. Kim, H. Lee, and J. Shin, "Guiding deep molecular optimization with genetic exploration," *Advances in neural information processing systems*, vol. 33, pp. 12 008–12 021, 2020.
- [18] C. Igel and M. Kreutz, "Operator adaptation in evolutionary computation and its application to structure optimization of neural networks," *Neurocomputing*, vol. 55, no. 1-2, pp. 347–361, 2003.
- [19] A. Topchy, W. F. Punch *et al.*, "Faster genetic programming based on local gradient search of numeric leaf values," in *Proceedings of the genetic and evolutionary computation conference (GECCO-2001)*, vol. 155162. Morgan Kaufmann San Francisco, CA, 2001.
- [20] A. Pourchot and O. Sigaud, "Cem-rl: Combining evolutionary and gradient-based methods for policy search," in *7th International Conference on Learning Representations, ICLR 2019*, 2019.
- [21] S. Khadka and K. Tumer, "Evolution-guided policy gradient in reinforcement learning," *Advances in Neural Information Processing Systems*, vol. 31, 2018.
- [22] M. J. Kusner, B. Paige, and J. M. Hernández-Lobato, "Grammar variational autoencoder," in *International conference on machine learning*. PMLR, 2017, pp. 1945–1954.
- [23] S. Sahoo, C. Lampert, and G. Martius, "Learning equations for extrapolation and control," in *International Conference on Machine Learning*. Pmlr, 2018, pp. 4442–4450.
- [24] S.-M. Udrescu and M. Tegmark, "Ai feynman: A physics-inspired method for symbolic regression," *Science advances*, vol. 6, no. 16, p. eaay2631, 2020.
- [25] P. W. Glynn and D. L. Iglehart, "Importance sampling for stochastic simulations," *Quality control and applied statistics*, vol. 36, no. 5, pp. 273–276, 1991.
- [26] P.-T. De Boer, D. P. Kroese, S. Mannor, and R. Y. Rubinstein, "A tutorial on the cross-entropy method," *Annals of operations research*, vol. 134, pp. 19–67, 2005.
- [27] Z. Liu, Y. Wang, S. Vaidya, F. Ruehle, J. Halverson, M. Soljačić, T. Y. Hou, and M. Tegmark, "Kan: Kolmogorov-arnold networks," *arXiv preprint arXiv:2404.19756*, 2024.
- [28] K. Xu, L. Chen, and S. Wang, "Kolmogorov-arnold networks for time series: Bridging predictive power and interpretability," *arXiv preprint arXiv:2406.02496*, 2024.
- [29] G. De Carlo, A. Mastropietro, and A. Anagnostopoulos, "Kolmogorov-arnold graph neural networks," *arXiv preprint arXiv:2406.18354*, 2024.
- [30] Z. Bozorgasl and H. Chen, "Wav-kan: Wavelet kolmogorov-arnold networks, 2024," *arXiv preprint arXiv:2405.12832*.
- [31] Z. Liu, P. Ma, Y. Wang, W. Matusik, and M. Tegmark, "Kan 2.0: Kolmogorov-arnold networks meet science," *arXiv preprint arXiv:2408.10205*, 2024.
- [32] A. Anaqreh, S.-K. Chou, I. Barašin, and C. Fortuna, "Towards automated and interpretable pathloss approximation methods," in *AAAI 2025 Workshop on Artificial Intelligence for Wireless Communications and Networking (AI4WCN)*, 2025.
- [33] B. Brik, H. Chergui, L. Zanzi, F. Devoti, A. Ksentini, M. S. Siddiqui, X. Costa-Pérez, and C. Verikoukis, "Explainable ai in 6g o-ran: A tutorial and survey on architecture, use cases, challenges, and future research," *IEEE Communications Surveys & Tutorials*, 2024.
- [34] S. Sun, T. S. Rappaport, S. Rangan, T. A. Thomas, A. Ghosh, I. Z. Kovacs, I. Rodriguez, O. Koymen, A. Partyka, and J. Jarvelainen, "Propagation path loss models for 5g urban micro-and macro-cellular scenarios," in *2016 IEEE 83rd Vehicular Technology Conference (VTC Spring)*. IEEE, 2016, pp. 1–6.
- [35] R. El Chall, S. Lahoud, and M. El Helou, "Lorawan network: Radio propagation models and performance evaluation in various environments in lebanon," *IEEE Internet of Things Journal*, vol. 6, no. 2, pp. 2366–2378, 2019.
- [36] R. J. Williams, "Simple statistical gradient-following algorithms for connectionist reinforcement learning," *Machine learning*, vol. 8, pp. 229–256, 1992.
- [37] D. A. Abolafia, M. Norouzi, J. Shen, R. Zhao, and Q. V. Le, "Neural program synthesis with priority queue training," *arXiv preprint arXiv:1801.03526*, 2018.
- [38] C.-L. Cheng, S. Kim, and A. Zajić, "Comparison of path loss models for indoor 30 ghz, 140 ghz, and 300 ghz channels," in *2017 11th European conference on antennas and propagation (EUCAP)*. IEEE, 2017, pp. 716–720.